Interface Barrier-Modulated Neuromorphic Behavior in Mo/CdIn2S4/ZnO–Al Structures Based on Metastable Defects

Jakub Zdzieblowski, Nicolas Barreau, Pawel Zabierowski

Interface barrier-modulated neuromorphic behaviour in $Mo/CdIn_2S_4/ZnO:Al$ structures based on metastable defects

Jakub Zdziebłowski[*a], *Nicolas Barreau*[b], *Paweł Zabierowski*[a].

[a]Faculty of Physics, Warsaw University of Technology, Koszykowa 75, 00-662 Warsaw, Poland

[b]Nantes Université, CNRS, Institut des Matériaux de Nantes Jean Rouxel, IMN, F-44000 Nantes, France

ABSTRACT Neuromorphic computing is an increasingly accelerating research field that still faces several hardware challenges, thus driving materials science research. This contribution presents prototype neuromorphic devices based on cadmium-indium sulphide ($CdIn_2S_4$). We have found that the compound, previously studied in photocatalysis and photovoltaics, has yet-to-be-explored memristive properties. We manufactured a series of devices with varying stoichiometry and unveiled their switching and neuromorphic behaviour. Our measurements indicate that barriers on the $CdIn_2S_4$ interfaces and native $CdIn_2S_4$ metastable defects control the behaviour of the devices. Due to its compelling optoelectronic properties, $CdIn_2S_4$ creates vast

* **Corresponding Author. Email: jakub.zdzieblowski@pw.edu.pl**

opportunities to use it as an active layer for optically controlled neuromorphic devices. We propose a disparate switching mechanism based on metastable defects that could be utilized in neuromorphic device technology.

KEYWORDS neuromorphic devices, memristive properties, semiconductor junction interfaces, chalcogenide semiconductors, metastable defects,

1. Introduction

Cadmium-indium sulfide ($CdIn_2S_4$) is a well-known n-type chalcogenide semiconductor with a spinel structure. Currently, the main area in which the material is being researched is its application in photocatalysis[1]. The vital role of $CdIn_2S_4$ has also been noticed in photovoltaics[2]. $CdIn_2S_4$ has also been found to have compelling photosensitive properties in the visible range[3,4], thus enabling its application in optoelectronics. It has also been found that the compound is rich in native defects[5,6]. The three most important that we will mention here are In_{Cd} antisites, called "T", that form the sub-bandgap density of states near the conduction band[5,7]; Cd_{In} acceptor states "E"[8]; and sulfur vacancies V_S - "V"[7]. It has been found that particular defect complexes, i.e. V-E are metastable[9]. However, most importantly, past research found effects characteristic of devices exhibiting memristive properties, i.e., resistive switching – abrupt resistivity change at a critical temperature[10] and memory effect – where the pinched hysteresis loop was spotted[11]. The observed properties were initially related to electrically induced conducting filaments, as well as to the presence of certain defects in the material. In particular, a giant hysteresis loop was observed in amorphous layers. Therefore, we started the research to investigate the possible

application of $CdIn_2S_4$ in neuromorphic devices. It is an intriguing research field, especially since the properties of the compound still need to be explored.

The switching phenomena observed in the past were the impetus for us to investigate cadmium-indium sulfide for application in neuromorphic devices. Herein, we present the first experimental neuromorphic device with $CdIn_2S_4$ as the active layer. We propose also an explanation of the switching mechanism which is based on the properties of metastable defects, and their impact on the interface barriers. Such defects exist in materials such as amorphous silicon[12], as well as in chalcopyrite semiconductors (anion vacancies)[13], and in AlGaAs (DX centers)[14]. These type of defects used to be an extensive research topic in solar cell technology[15]. The mentioned V-E in $CdIn_2S_4$ was found theoretically to have such properties. Although the action of our devices might resemble interface switching behaviour observed in other structures[16–24], our model, based on metastable defects, is grounded on the current state of $CdIn_2S_4$ knowledge[9], and aligns best with observations, providing an elegant explanation.

2. Device fabrication and characterization

Polycrystalline $CdIn_2S_4$ thin films, of a thickness of about 400nm, were deposited through the simultaneous evaporation of CdS, In and S on soda lime glass substrates coated with sputtered molybdenum (SLG/Mo). The fluxes of CdS and In were set such that the composition of the completed layers grown on substrates heated at 200°C, corresponds to $CdIn_2S_4$. One should notice that the substrate temperature during the deposition has been used to control the Cd content of the layer. In fact, substrates temperature above 250°C yields a partial re-evaporation of CdS, this CdS loss increases with substrate temperature. These structures were then covered with 400 nm polycrystalline AZO:Al layer (AZO), deposited by RF sputtering from a ceramic

target (wt.%Al_2O_3 of 3%). Wide-bandgap AZO acts as a transparent electrode, enabling the illumination of the $CdIn_2S_4$ active layer with energies below its bandgap, which correspond to wavelengths higher than ~350 nm. Finally, aluminium electrodes were deposited using the electron beam evaporation through a shadow mask. All investigated structures consist of two rectifying contacts: a Schottky junction at the Mo/C24 interface and a n/n^{++} junction at the $CdIn_2S_4$/AZO interface, as schematically presented in Fig. 1. We manufactured devices with diverse In/Cd atomic ratios, namely 5, 2.5, and 1.86 because this relative content of cations is known significantly impact the overall optoelectronic properties of $CdIn_2S_4$[3,6,25,26], in particular those investigated herein.

The at. In/Cd ratio, was determined by Energy Dispersive X-Ray Spectroscopy (EDX) using a SEM (JEOL JSM 5800LV) equipped with a SAMx SDD energy dispersive spectrometer.

Complete devices were measured using a Keithley 2450 SMU in the function of temperature and sweep rate. Mo side was arbitrarily set as a reference. We applied a train of triangular cyclic voltage sweeps starting and ending at 0V, which allowed us to observe switching and collect the hysteresis loop. Next, we moved towards the neuromorphic-oriented experiments, i.e. pulse potentiation and paired-pulse facilitation. We applied a train of square pulses using Keithley 2450 and recorded the current using a custom-built transimpedance amplifier and an ADC card.

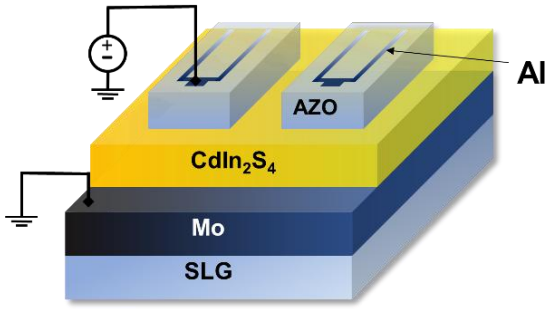

Figure 1. Structure of the devices. The molybdenum layer, sputtered on the soda-lime glass, acts as a bottom electrode. Then, $CdIn_2S_4$ with various compositions (i.e. at.Cd/In ratio) were grown by co-evaporation. A sputtered AZO layer covered with Al top contacts completes the device.

Secondly, we applied light pulses using a 460nm LED with a power density of 4mW/cm^2 as a light source and a mechanical shutter (Thorlabs SC10).

We note that we have carefully tested the configuration of the layers without $CdIn_2S_4$, i.e. the Mo/AZO structure, and did not find any switching behaviour; thus, we infer that all switching and neuromorphic-related effects originate from $CdIn_2S_4$.

3. Material characterization - persistent photoconductivity

To thoroughly investigate metastable phenomena in the $CdIn_2S_4$ (abbrev. C24), we meticulously prepared the $CdIn_2S_4$ thin-films grown on soda lime glass substrates in a lateral configuration with Ni:Al contacts for detailed electrical characterization. For the measurement, samples were mounted in Janis liquid nitrogen-cooled cryostat in vacuum (pressure $<10^{-8}$ bar), and measured using Keithley 2450. The possible barrier at the metal-semiconductor junction (C24/Ni:Al) is negligible, because the entire applied voltage drops across the bulk of the material. This ensures that our measurements accurately reflect the intrinsic resistance of the C24 material itself. These were layers of the target material that was subsequently integrated into our devices. Our primary approach involved measuring the conductivity of the C24 thin-films as a function of temperature. This fundamental measurement allows us to probe the metastable properties. The theory predicts that V-E defects are metastable, with a transition energy of 0.4 eV below the conduction band minimum[9]. These defects can metastably capture holes and electrons which requires activation over internal structural energy barriers. This phenomenon is typically accompanied by Persistent Photoconductivity (PPC), and indeed, we observe this effect in our layers. Fig. 2 illustrates the temperature dependence of relaxed conductivity and the effect of PPC after light soaking which was performed either at low temperature (LNT in Fig. 1) or during

cooling (EWC in Fig. 1), i.e. conductivity was measured after switching the light off. For light soaking, we used monochromatic light (460nm, 4 mW/cm^2). Notably, residual PPC is observable even at 300K, highlighting the robust nature of these metastable defects. Furthermore, as discussed below, the presence of metastable defects sufficiently explains the switching effect of our devices, both under voltage and light illumination.

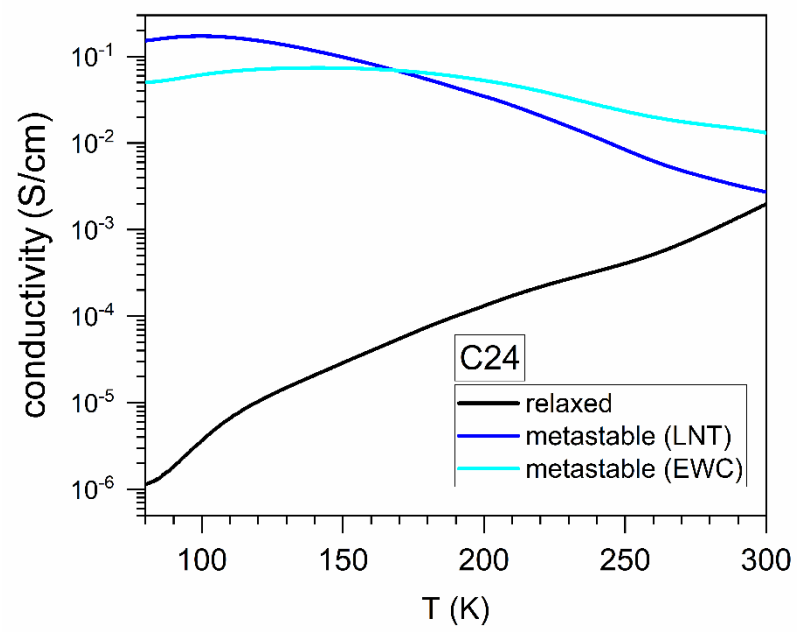

Figure 2. Conductivity vs temperature measurement of the C24 thin film in the relaxed state and light-soaked state. The light soaking was performed using 460nm 4mW/cm^2 monochromatic light. The procedure was performed either during cooling from room temperature down to liquid nitrogen temperature (excitation while cooling, EWC) or in liquid nitrogen temperature for 15min. (LNT). The metastable effect induced by EWC persist up to room temperature with the conductivity increased by one order of magnitude.

4. Results

The manufactured device is composed of two rectifying contacts with opposite directions: a Schottky junction between molybdenum and $CdIn_2S_4$, and an n-type isotype junction between $CdIn_2S_4$ and AZO. As molybdenum and an n^{++}-AZO have comparable work

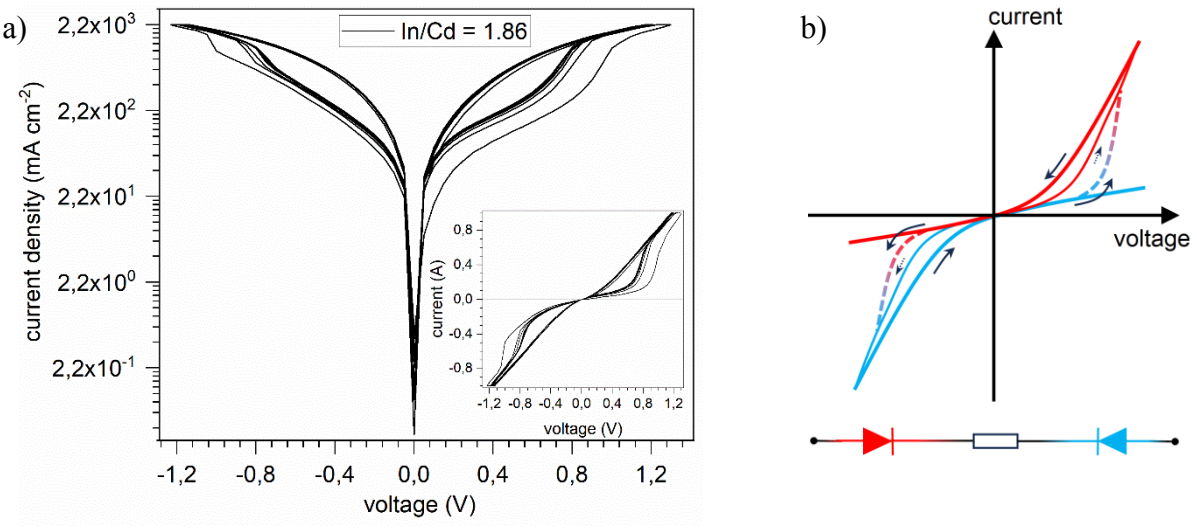

Figure 3. I–V characteristics and switching mechanisms of the devices. a) Representative semilog I–V characteristics of the device with $CdIn_2S_4$ layer close to stoichiometry (In/Cd = 1.86). Inset shows the same I–V curve with a linear scale, which can be compared to the schematic in Fig. 3b. b) Principle of switching: The A and B states are traced in Fig. 3b with red and blue colours, respectively. The A and B states originate form two rectifying junctions in opposing directions. When the device is in state B, it will switch to state A when sufficient positive voltage is applied and vice versa when negative voltages are applied. When there is no state A – state B switch (e.g., when the polarity matches the device's current state or, the sweep is unipolar or the sweep amplitude below the switch voltage), the device stays in one regime. However, a second smaller hysteretic behaviour will still be observed, which is also shown in Fig. 3b (thin curves) and visible in Fig. 3a. and 4.

functions, the heights of the barriers at both junctions are comparable. The complete structure is shown in Fig. 1. By applying an arbitrary triangle waveform, we can clearly observe the pinched hysteresis loop, which can be considered as a fingerprint for memristive devices[27]. The shape of hysteresis loop was roughly similar in all fabricated devices. The typical IV–hysteresis loop is shown in Fig. 3a. This is a so-called tangential or non-transversal pinched hysteresis loop[28]. By carefully analyzing the shape and the evolution of the I–V loop, we can deduce the basic mechanism behind the switching behaviour.

The direction and evolution of the I–V curve are schematically shown in Fig. 3b. The device and, as a result, its I–V characteristics can be considered as two diodes with variable barriers connected in opposite directions. The switching occurs between two conductivity regimes: the state A regime (represented in red) when the barrier on AZO is reduced, and the state B regime (blue) when the barrier on molybdenum is diminished. Those two regimes can be considered as if the device has only one rectifying junction and some series resistance. When a voltage with a polarity opposite to the current regime is applied (e.g. the device in state B regime and a positive voltage is applied), the device will switch at a specific threshold voltage range. With approximate work functions of the used compounds in mind, we propose a band diagram of the devices (Fig. 4), showing the detailed principle of operation. At low positive voltage, the AZO/$CdIn_2S_4$ junction becomes positively biased. The opposing barrier ($CdIn_2S_4$/Mo junction) gradually diminishes (point **a** on Fig. 4) around the threshold voltage. When the barrier on molybdenum is fully minimized (state A, point **b**), the device exhibits close to ohmic resistivity (AZO/$CdIn_2S_4$ junction is strongly forward-biased). At lower voltages in the state A (during the return), the AZO/$CdIn_2S_4$ barrier begins to dominate, and takes over when the barrier top becomes higher than the Mo level (point **c**). When the voltage changes sign, the mirror process

begins, where barriers are swapped, and $CdIn_2S_4$/Mo barrier is reduced. Hence, at point **d** in Fig.

4 the bias enters the threshold voltage range, and the AZO/$CdIn_2S_4$ barrier reduces. The device

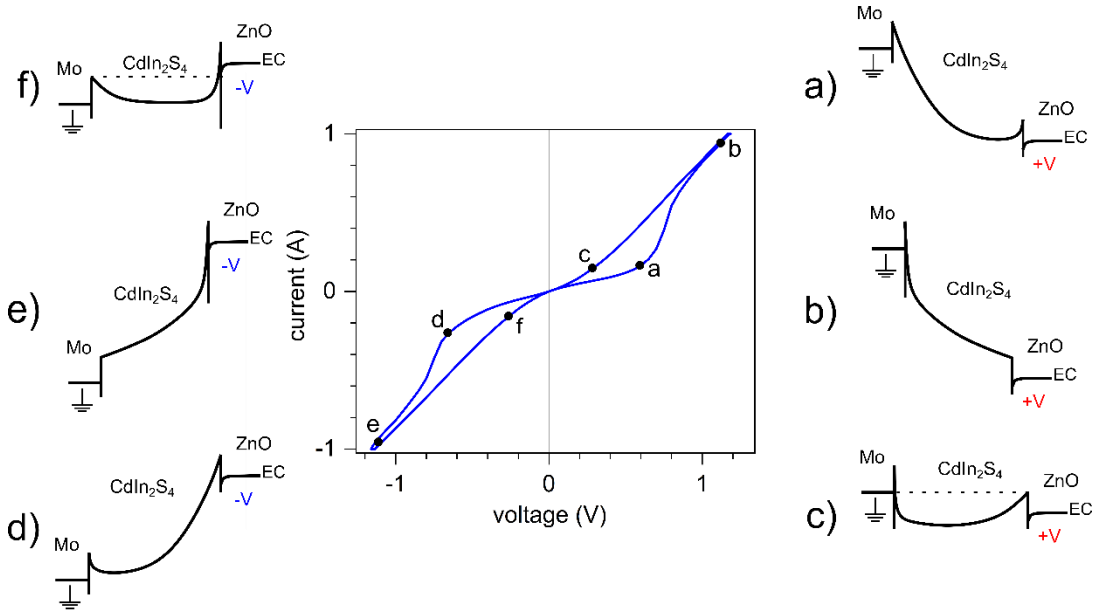

Figure 4. Schematical bands (conduction band) profiles at characteristic points on the I–V characteristic of stochiometric sample (In/Cd = 1.86): a) Transition region from state B to state A, b) state A with fully reduced barrier on Mo, c) state A with AZO barrier blocking, d) Transition region from state A to state B, e) state B with fully reduced barrier on AZO, f) state B with Mo barrier blocking. The switching is based on the minimization of one of the barriers (narrowing the space-charge region). At transition region (point a), transport is controlled by both junctions (Mo junction is reversely biased). In state A (b) barrier on Mo is fully reduced and barrier on AZO is deeply conduction biased resulting in close to ohmic conduction state of the device. At lower positive bias (c), barrier on AZO becomes limiting again after the threshold point schematically shown in diagram c. At negative bias, similar mechanism occurs with junction roles reversed.

voltages, when the top of the $CdIn_2S_4$/Mo barrier extends over the AZO level, the barrier begins

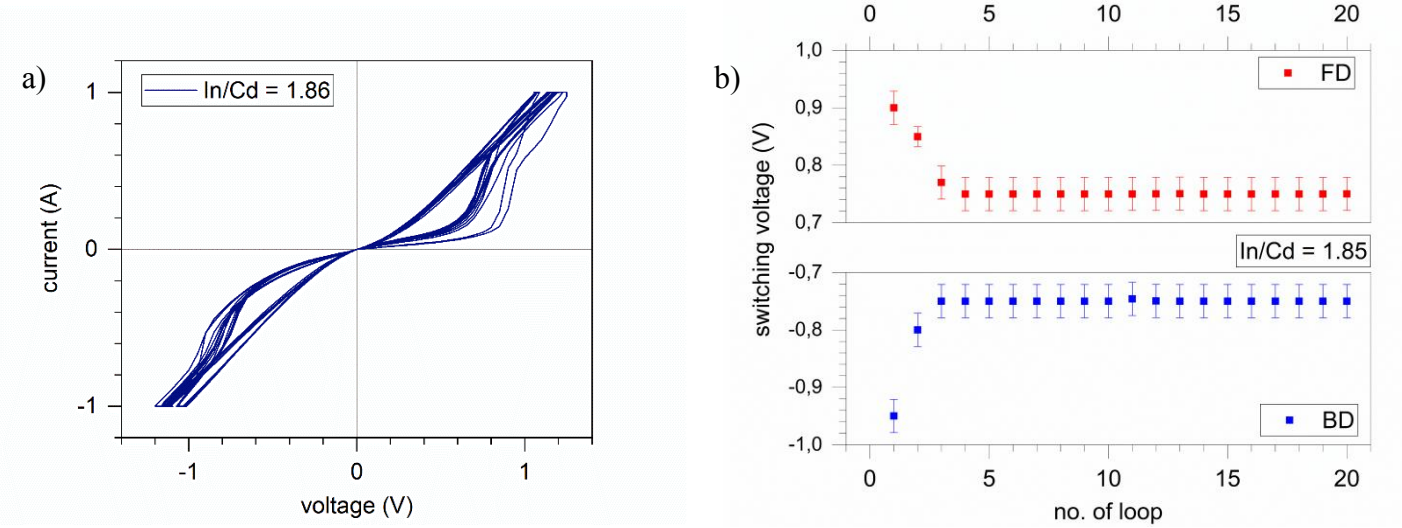

Figure 5. Repetitive switching behaviour of the device. a) Overlay of 20 consecutive hysteresis loops measured for a sample with In/Cd = 1.86. b) Extracted switching voltage states and B as a function of cycle number, derived from the derivative of the voltage curves. After the initial two cycles, the device exhibits stable operation.

to control the conductivity.

Within the described operation, there is a mechanism of voltage-induced barrier reduction required to explain the switching phenomena. Note that the switching event is not instantaneous but requires finite time/charge to fully get on the alternative path (dotted lines in Fig. 3b). The switching time is related to the total current (charge) flow through the device (which is indicated by current response when a train of pulses is being applied). Therefore, some charging/recharging effect governs the behaviour. This effect is also a source of the neuromorphic behaviour of the devices. Altering barrier height at one side resets the state on the

other, and the device effectively switches between the states A and B. To explain this phenomenon, we propose a model which involves the influence of metastable sulfur vacancies, as explained in more detail in the next section.

To thoroughly investigate the repeatability of the switching effect, we conducted measurements of the hysteresis loops, performing twenty consecutive cycles. Figure 5a shows a representative set of these measurements for a sample with an In/Cd =1.86. From these multiple cycles, we determined the switching voltage to the A and B states, using the derivative method. The calculated switching voltage is shown in Fig. 5b. Our analysis clearly demonstrates that, after the initial two cycles, the switching voltage remains remarkably stable despite repeated cycling, indicating good device endurance.

To assess the memory retention capabilities of the devices, we measured the stability of both

the high resistance state (state A) and the low resistance state (state B) over time. These retention

measurements were performed for samples with In/Cd ratios: 5, 2.5, and 1.85. The results,

presented in Fig. 6, demonstrate that while the devices exhibit some retention, the observed

memory window is currently limited. This is primarily attributed to the fact that these measurements were conducted at room temperature and on unoptimized devices. Crucially, the

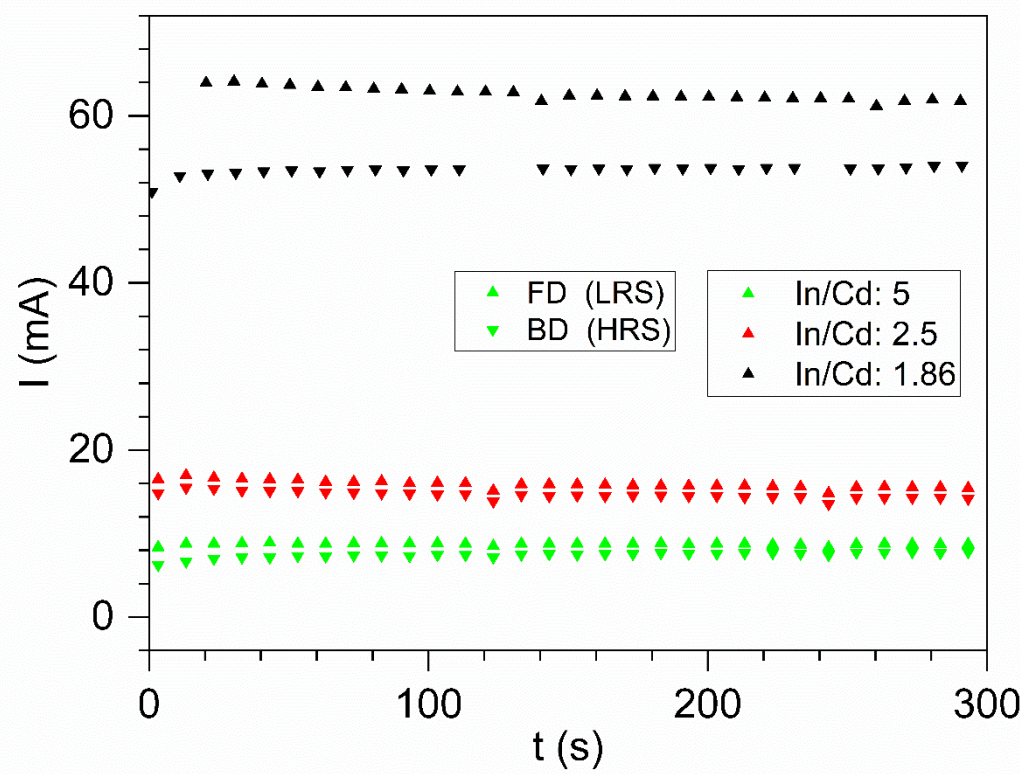

Figure 6. Retention characteristics of the devices. Stability of the A and B state for devices with varying In/Cd ratios (5, 2.5, and 1.85) over time. The readout voltage was kept below 0.25V to prevent the devices from switching.

readout voltage was set to 0.25V. This low voltage was necessitated by the proximity of the switching voltage, but it inherently restricts the discernible difference between the high and low resistance states, thereby contributing to the seemingly modest retention performance. Further optimization of device architecture and material properties is expected to significantly improve retention characteristics. Given that the neuromorphic properties are inherently linked to the characteristics of $CdIn_2S_4$, it can be anticipated that optimizing the barrier through careful electrode selection will yield significantly improved neuromorphic performance.

By applying a train of square 10ms pulses with an amplitude that matches the threshold voltage of the state A – state B, the device will gradually switch from one state to another, increasing current and practically realizing synaptic potentiation. Fig. 7a shows typical current evolution under a sequence of potentiation pulses with an amplitude of 0.5V, applied to a device with the In/Cd ratio close to stoichiometry (In/Cd = 1.86). We gradually modulate the device resistivity, initially in state B, towards the state A. The current tends asymptotically to the value of the current in the state A corresponding to the value of the applied voltage.

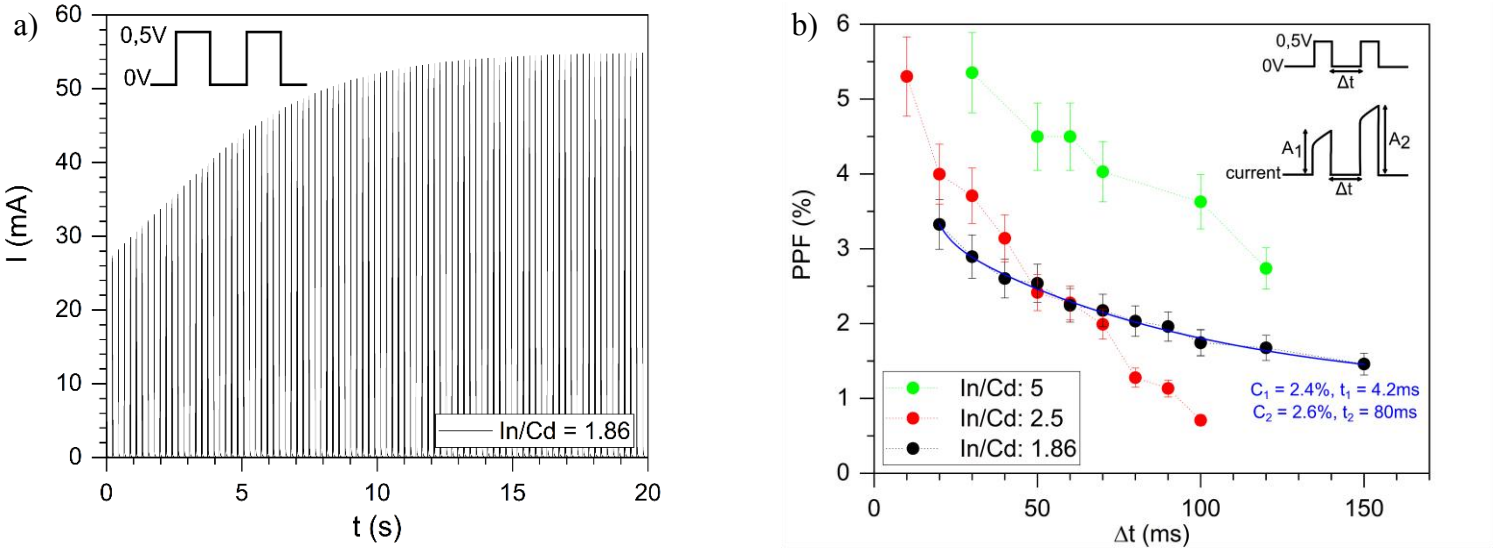

Figure 7. Neuromorphic behaviour of the devices. a) Synaptic potentiation behaviour was observed in the device, with the In/Cd ratio close to stochiometric. Voltage pulses modulate the current value. The current is modulated in the range between values in A and B states at a given pulse voltage. b) PPF behaviour for devices with CdIn2S4 having an In/Cd ratio. A fit was performed for In/Cd = 1.86, yielding amplitudes and decay constants for long-term and short-term memory.

To investigate the potentiation phenomena further, we applied trains of 0.5V pulses with different timings to all devices from the series with stoichiometry deviations, realizing classical paired-pulse facilitation synaptic plasticity. We varied the delay Δt between pulses in the range of 10-150ms, keeping constant pulse duration (10ms) and amplitude (0.5V). Having the first pulse amplitude A1 and concurrent pulse amplitude A2, we can calculate the PPF function as follows:

$$PPF\ [\%] = \frac{A_2 - A_1}{A_1} 100\%$$

The PPF is found to follow a double exponential function:

$$PPF = \mathrm{C}_1 \exp\left(-\frac{t}{t_1}\right) + \mathrm{C}_2 \exp\left(-\frac{t}{t_2}\right)$$

Where C1, C2 are initial magnitudes and t_1, t_2 are fast and slow decay constants, respectively. The fast component can be related to the short-term plasticity (STP), and the slow component – to the long-term plasticity (LTP). For the sample with an In/Cd ratio close to stoichiometric, we fitted the PPF double exponential function. We obtained values for LTP and STP, given 2.4% and 2.6% amplitudes and 4.2ms and 80ms decay constants for STP and LTP, respectively.

We repeated the PPF experiment on devices with various $CdIn_2S_4$ stoichiometries. Fig. 7b shows a comparison of the PPF behaviour for the tested samples. We observe a distinct dependence of amplitudes and time constants on Cd/In ratio. Although the detailed impact of stoichiometry on sample behavior is unknown, we observe a trend towards a desired higher PPF response. Hence, further optimizations are possible.

For the sample with In/Cd = 1.86 under 0.25V bias, we performed optical potentiation using

460nm, 100ms, 2mW/cm^2 pulses, in an analogous manner to previously applied electrical

potentiation (Fig. 8). To further investigate the optical potentiation mechanism, we conducted a

series of potentiation cycles, or "epochs," of light stimulation, each with 10 light pulses (Fig. 8a).

This allowed us to observe the cumulative effect of repeated light pulses on the device's

conductivity and to better understand the dynamics of photo-induced memory states. The low

resistivity persists long after the light source is turned off, indicating the presence of Persistent

Photoconductivity (PPC). The light-induced switching differs from electrical switching between A and B states because optical stimulation simultaneously turns both diodes into a low resistivity

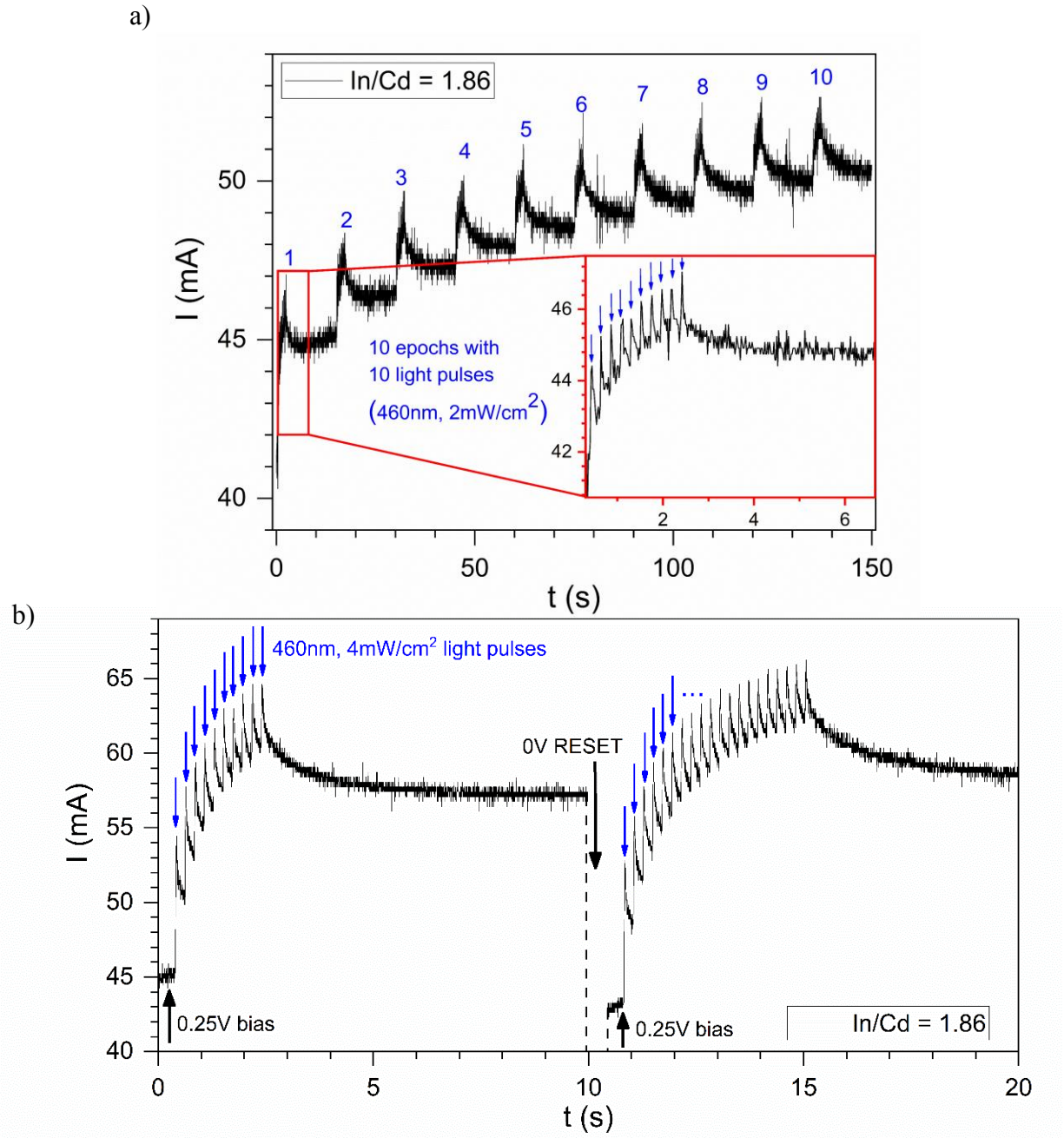

Figure 8. Optical stimulation of the device with In/Cd = 1.86. a) Ten consecutive cycles of optical stimulation containing a train of ten 460nm light pulses with 100ms duration in each cycle. A persistent photoconductivity is observed. Short-term and long-term memory components are visible during the current relaxation after light pulses. b) Reproducible optical potentiation of the device. Two cycles of light-induced potentiation changes are shown, with the device effectively reset to its baseline state by applying 0V between cycles.

state. We note that it is possible to reset the device from the optically stimulated state, by removing the electrical bias, i.e. by applying 0V to the device. To specifically demonstrate and confirm the reset mechanism, we intentionally designed an experiment where the device was reset by applying 0V between two successive potentiation cycles (Fig. 8b). This experiment demonstrates the ability to control the device's memory states and serves as a vital method for re-establishing the initial high resistivity state. Currently, other known reset methods include heating the device to 60°C, applying a voltage of opposite polarity, or waiting a sufficiently long time.

5. Discussion

We propose a basic explanation of the switching mechanism and resulting neuromorphic behaviour based on interface barrier modulation governed by metastable defect complexes present in $CdIn_2S_4$. The V-E (V_S-Cd_{In}) defect complex exhibits metastability due to large lattice relaxation during carrier capture. This leads to multiple stable or metastable configurations with distinct charge states and optoelectronic properties. Since the $CdIn_2S_4$ Fermi level is close to the conduction band, the V-E complex is in a negative charge state, i.e. it is occupied with two electrons. In this state, the defect can capture two holes, convert into a positive charge state, which is accompanied by a large lattice relaxation. In the positive charge state, there is a potential barrier for the hole emission (or electron capture) and the relaxation into the original state is persistently blocked.

Now we extend the proposed band diagram of the devices from Fig. 4 including the spatial distribution of metastable defects (Fig. 9). In the $CdIn_2S_4$ layer, we drew two energy levels representing the V-E metastable defect complex in the negative (lower) and positive (upper)

charge states. Then, we marked V-E defects in one of the particular states, as shown in the

legend. The mechanism goes as follows: In the $CdIn_2S_4$ layer, there is some non-uniform spatial

distribution of V-E defects in positive and negative charge states. Naturally, the defects' charge

participates in the band bending: defects in a positive charge state near one of the barriers, increase the electrical field and, therefore, increasing the tunnelling current, practically short-circuit one of the junctions. The distribution of the charge states can be changed by applying an external electric field, lowering the charge emission potential barrier from the defect, and charge redistribution through hopping or drift. Hence, a specific threshold voltage is observed, and switching takes finite time as the redistributing charge modulates spatial occupation distribution and, therefore, band bending. The A and A states results from the two extreme situations, where the opposite charge states are fully polarized. Neuromorphic behaviour observed while applying

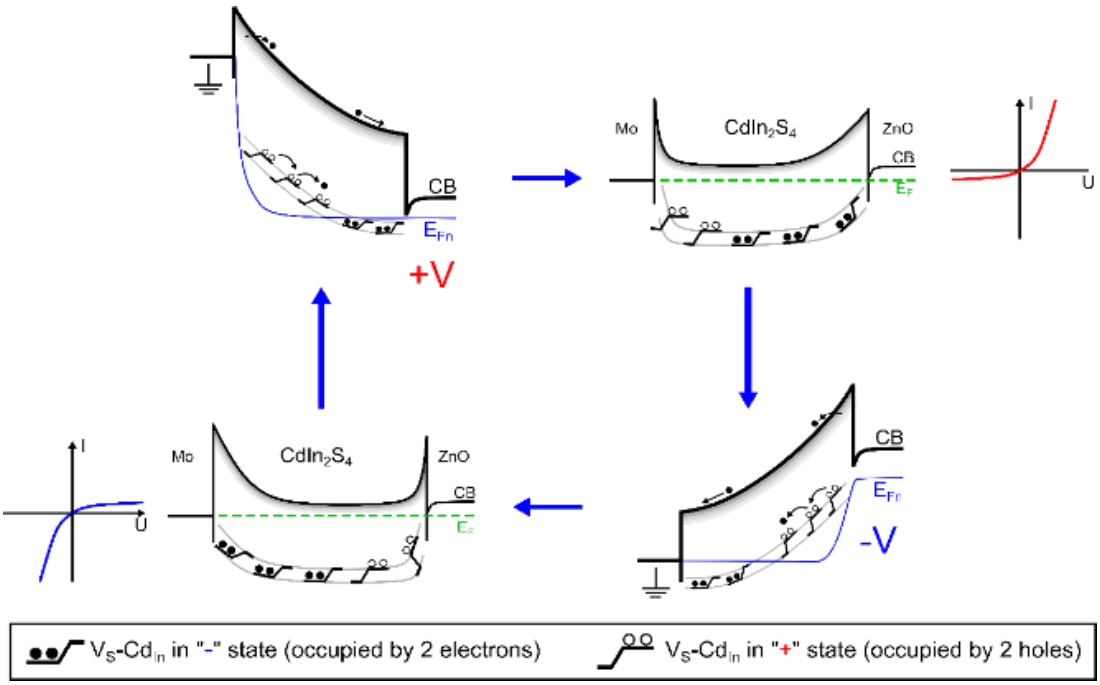

Figure 9. Schematic representation of the band diagrams of the device in the state A (upper right), state B (lower left), and transition state when electric field is applied. The defect levels and charge states are schematically marked. Minimalizing one of the barriers caused by defects in the positive charge state results in a large tunnelling current through the potential barrier and practically shorting the rectifying junction.

a train of pulses originates from the piecemeal change of the spatial occupation function and gradual barrier modulation. The hysteresis loop directly results from the modulation of the spatial distribution function of the defect charge state. A small hysteresis loop observed in one of the two regimes (state A, state B) may result from a similar mechanism, but with the T states involved. The T states, the quasi-continuous distribution of states is marked as a gradient shadow below CB in Fig. 9.

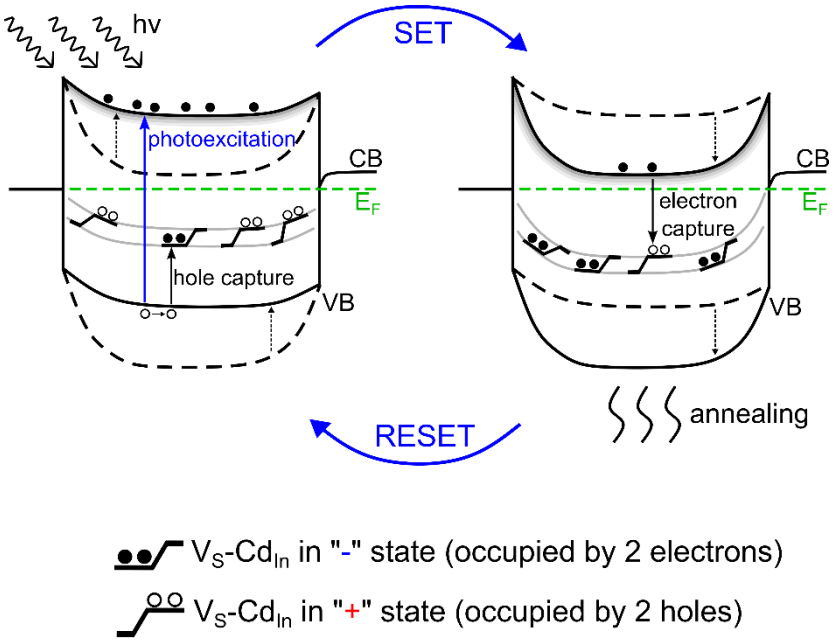

Figure 10. Schematic representation of the device's band diagram during optical potentiation. Incident light generates an e-h pair; holes are captured by the metastable defects, causing large lattice relaxation and charge state change. As a result, a persistent photoconductivity is observed.

Hole capture by the V-E complex can also be induced optically, thus enabling a similar mechanism of optical potentiation (Fig. 10). Free holes generated in band-to-band excitation are captured by V-E defects. This causes band bending and decreases overall device resistivity.

Applying light pulses will, therefore, gradually decrease total device resistivity. During the annealing, the captured holes can overcome the lattice relaxation barrier and recombine with the electrons, restoring the initial state.

6. Conclusions

We have manufactured the first working memristive devices based on $CdIn_2S_4$. We performed an exploratory electrical and optical characterization and proposed a basic explanation of the switching and neuromorphic behavior. The proposed metastable defects-based mechanism can fully explain the switching between states A and B within itself, and its foundation lies in past research of the $CdIn_2S_4$[9]. We have not observed any additional effects challenging the current explanation, although more research (i.e. capacitance spectroscopy) is required.

While our current retention data at room temperature shows some limitations, it's important to recognize that these measurements were performed on unoptimized devices and at a necessarily constrained readout voltage of 0.25V, due to the proximity of the switching voltage. We anticipate that further optimization of the device architecture and material engineering will significantly enhance these characteristics, leading to improved memory window and retention performance.

It should be noted that increasing barrier heights would result in amplifying the switching amplitude, i.e. the difference between state A and state B, and also in larger potentiation abilities, as we extend the possible range of barrier heights.

The results will serve as a basis for further exploration of $CdIn_2S_4$-based devices with the milestone of incorporating metastable defects. The results also pave the way toward further

optimization, including enhancing neuromorphic response. We expect that more intricate defect manipulation, i.e. increasing the density of sulfur vacancies while decreasing non-beneficial defects concentration, will boost the device performance, as well as further interface manipulation, i.e. replacing AZO or molybdenum with compounds with larger work function.

The possibility of utilizing the optoelectronic properties of $CdIn_2S_4$, particularly metastable defects, opens new opportunities for constructing novel types of memristive devices, including all-optically controlled (AOC) memristors. This work is a first step towards this goal.

ASSOCIATED CONTENT

Supporting Information. No supporting information.[29]

Author Contributions

The manuscript was written through contributions of all authors. All authors have given approval to the final version of the manuscript.

Funding Sources

In Poland the studies were funded by ENERGYTECH-1 project granted by Warsaw University of Technology under the program Excellence Initiative: Research University (ID-UB).

Notes

-

ACKNOWLEDGMENT

The authors gratefully acknowledge The Innovative materials for optics, photovoltaic and storage (MIOPS) group from Institut des Matériaux de Nantes Jean Rouxel (IMN), Nantes,

France for providing the necessary technological resources for synthesizing cadmium-indium sulfides.

ABBREVIATIONS

LTP, long-term plasticity; STP, short-term plasticity; PPF, paired-pulse potentiation.

REFERENCES

(1) Chandrasekaran, S.; Bowen, C.; Zhang, P.; Li, Z.; Yuan, Q.; Ren, X.; Deng, L. Spinel Photocatalysts for Environmental Remediation, Hydrogen Generation, CO_2 Reduction and Photoelectrochemical Water Splitting. *J. Mater. Chem. A* **2018**, *6* (24), 11078–11104. https://doi.org/10.1039/C8TA03669A.

(2) Barreau, N.; Frelon, A.; Lepetit, T.; Gautron, E.; Gautier, N.; Ribeiro- Andrade, R.; Nicoara, N.; Sadewasser, S.; Zabierowski, P.; Arzel, L.; Choubrac, L.; Harel, S.; Deudon, C.; Latouche, C.; Jobic, S.; Caldes, M.; Assmann, L.; Tsoulka, P.; Péan, E. V.; Lorthioir, J.; Geschier, F.; Braems, I.; Moret, M.; Briot, O.; Ouvrard, G. High Efficiency Solar Cell Based on Full PVD Processed Cu(In,Ga)Se_2/$CdIn_2S_4$ Heterojunction. *Solar RRL* **2017**, *1* (11), 1700140. https://doi.org/10.1002/solr.201700140.

(3) Nakanishi, H.; Miyashita, H.; Endo, S.; Irie, T. Photoluminescence and Photoconduction in the System $(CdIn_2S_4)_{1-x}$-$(In_2S_3)_x$. *Jpn. J. Appl. Phys.* **1981**, *20* (8), 1481. https://doi.org/10.1143/JJAP.20.1481.

(4) Charlebois, A.; Fortin, E. Gain Excitation Spectrum and Acceptor Density in $CdIn_2S_4$. *Journal of Applied Physics* **1989**, *66* (7), 3220–3223. https://doi.org/10.1063/1.344139.

(5) Anedda, A.; Garbato, L.; Raga, F.; Serpi, A. Photoconductivity and Trap Distribution in CdIn2S4. *Phys. Stat. Sol. (a)* **1978**, *50* (2), 643–650. https://doi.org/10.1002/pssa.2210500234.

(6) Georgobiani, A. N.; Gruzintsev, A. N.; Ratseev, S. A.; Tezlevan, V. E.; Tiginyanu, I. M.; Ursaki, V. V. Luminescence and Photoconductivity Caused by Antisite Defects in $CdIn_2S_4$ Single Crystals. *Cryst. Res. Technol.* **1986**, *21* (2), 259–263. https://doi.org/10.1002/crat.2170210218.

(7) Charbonneau, S.; Fortin, E.; Anedda, A. Saturation Photoconductivity in CdIn 2 S 4. *Phys. Rev. B* **1985**, *31* (4), 2326–2329. https://doi.org/10.1103/PhysRevB.31.2326.

(8) Grilli, E.; Guzzi, M.; Cappelletti, P.; Moskalonov, A. V. Photoluminescence of CdIn2S4 Single Crystals Recombination Process and Localized Levels. *Phys. Stat. Sol. (a)* **1980**, *59* (2), 755–765. https://doi.org/10.1002/pssa.2210590243.

(9) Péan, E. V.; Barreau, N.; Vidal, J.; Latouche, C.; Jobic, S. Theoretical Investigation of CdI n 2 S 4 : A Possible Substitute for CdS in CuIn1-xGaxSe2-Based Photovoltaic Devices. *Phys. Rev. Materials* **2017**, *1* (6), 064605. https://doi.org/10.1103/PhysRevMaterials.1.064605.

(10) Seki, Y.; Endo, S.; Irie, T. Switching Phenomena in CdIn2S4 Thin Films. *Il Nuovo Cimento D* **1983**, *2* (6), 1846–1851. https://doi.org/10.1007/BF02457875.

(11) Ueno, M.; Endo, S.; Irie, T. Memory Effects of $CdIn_2S_4$ Single Crystal. *Jpn. J. Appl. Phys.* **1974**, *13* (3), 580–580. https://doi.org/10.1143/JJAP.13.580.
(12) Baraff, G. A.; Kane, E. O.; Schlüter, M. Theory of the Silicon Vacancy: An Anderson Negative- U System. *Phys. Rev. B* **1980**, *21* (12), 5662–5686. https://doi.org/10.1103/PhysRevB.21.5662.
(13) Lany, S.; Zunger, A. Anion Vacancies as a Source of Persistent Photoconductivity in II-VI and Chalcopyrite Semiconductors. *Phys. Rev. B* **2005**, *72* (3), 035215. https://doi.org/10.1103/PhysRevB.72.035215.
(14) Mooney, P. M. Electrical Properties of DX Centers in GaAs and AlGaAs. *Radiation Effects and Defects in Solids* **1989**, *111–112* (1–2), 281–298. https://doi.org/10.1080/10420158908213003.
(15) Igalson, M.; Maciaszek, M.; Macielak, K.; Czudek, A.; Edoff, M.; Barreau, N. Concentration of Defects Responsible for Persistent Photoconductivity in Cu(In,Ga)Se2: Dependence on Material Composition. *Thin Solid Films* **2019**, *669*, 600–604. https://doi.org/10.1016/j.tsf.2018.11.038.
(16) Chen, A.; Zhang, W.; Dedon, L. R.; Chen, D.; Khatkhatay, F.; MacManus- Driscoll, J. L.; Wang, H.; Yarotski, D.; Chen, J.; Gao, X.; Martin, L. W.; Roelofs, A.; Jia, Q. Couplings of Polarization with Interfacial Deep Trap and Schottky Interface Controlled Ferroelectric Memristive Switching. *Adv Funct Materials* **2020**, *30* (43), 2000664. https://doi.org/10.1002/adfm.202000664.
(17) Gao, S.; Liu, G.; Yang, H.; Hu, C.; Chen, Q.; Gong, G.; Xue, W.; Yi, X.; Shang, J.; Li, R.-W. An Oxide Schottky Junction Artificial Optoelectronic Synapse. *ACS Nano* **2019**, *13* (2), 2634–2642. https://doi.org/10.1021/acsnano.9b00340.
(18) Xi, F.; Han, Y.; Liu, M.; Bae, J. H.; Tiedemann, A.; Grützmacher, D.; Zhao, Q.-T. Artificial Synapses Based on Ferroelectric Schottky Barrier Field-Effect Transistors for Neuromorphic Applications. *ACS Appl. Mater. Interfaces* **2021**, *13* (27), 32005–32012. https://doi.org/10.1021/acsami.1c07505.
(19) Li, S.; Li, B.; Feng, X.; Chen, L.; Li, Y.; Huang, L.; Fong, X.; Ang, K.-W. Electron-Beam-Irradiated Rhenium Disulfide Memristors with Low Variability for Neuromorphic Computing. *npj 2D Mater Appl* **2021**, *5* (1), 1. https://doi.org/10.1038/s41699-020-00190-0.
(20) Tan, H.; Liu, G.; Yang, H.; Yi, X.; Pan, L.; Shang, J.; Long, S.; Liu, M.; Wu, Y.; Li, R.-W. Light-Gated Memristor with Integrated Logic and Memory Functions. *ACS Nano* **2017**, *11* (11), 11298–11305. https://doi.org/10.1021/acsnano.7b05762.
(21) Li, D.; Wu, B.; Zhu, X.; Wang, J.; Ryu, B.; Wei, L.; Liang, X. MoS2 Memristors Exhibiting Variable Switching Characteristics toward Biorealistic Synaptic Emulation. *ACS Nano* **2018**, No. 12, 9240−9252. https://doi.org/10.1021/acsnano.8b03977.
(22) Gaggio, B.; Jan, A.; Muller, M.; Salonikidou, B.; Bakhit, B.; Hellenbrand, M.; Di Martino, G.; Yildiz, B.; MacManus-Driscoll, J. L. Sodium-Controlled Interfacial Resistive Switching in Thin Film Niobium Oxide for Neuromorphic Applications. *Chem. Mater.* **2024**, *36* (11), 5764–5774. https://doi.org/10.1021/acs.chemmater.4c00965.
(23) Hansen, M.; Ziegler, M.; Kolberg, L.; Soni, R.; Dirkmann, S.; Mussenbrock, T.; Kohlstedt, H. A Double Barrier Memristive Device. *Sci Rep* **2015**, *5* (1), 13753. https://doi.org/10.1038/srep13753.
(24) You, T.; Du, N.; Slesazeck, S.; Mikolajick, T.; Li, G.; Bürger, D.; Skorupa, I.; Stöcker, H.; Abendroth, B.; Beyer, A.; Volz, K.; Schmidt, O. G.; Schmidt, H. Bipolar Electric-Field

Enhanced Trapping and Detrapping of Mobile Donors in BiFeO 3 Memristors. *ACS Appl. Mater. Interfaces* **2014**, *6* (22), 19758–19765. https://doi.org/10.1021/am504871g.
(25) Czaja, W.; Krausbauer, L. Photoluminescence of CdIn2S4 and Mixed Crystals with In2S3 as Related to Their Structural Properties. *phys. stat. sol. (b)* **1969**, *33* (1), 191–199. https://doi.org/10.1002/pssb.19690330116.
(26) Seminovski, Y.; Palacios, P.; Wahnón, P.; Grau-Crespo, R. Band Gap Control via Tuning of Inversion Degree in Cdin 2 s 4 Spinel. *Appl. Phys. Lett.* **2012**, *100* (10), 102112. https://doi.org/10.1063/1.3692780.
(27) Adhikari, S. P.; Sah, M. Pd.; Kim, H.; Chua, L. O. Three Fingerprints of Memristor. *IEEE Trans. Circuits Syst. I* **2013**, *60* (11), 3008–3021. https://doi.org/10.1109/TCSI.2013.2256171.
(28) Biolek, D.; Biolek, Z.; Biolkova, V.; Kolka, Z. Some Fingerprints of Ideal Memristors. In *2013 IEEE International Symposium on Circuits and Systems (ISCAS2013)*; IEEE: Beijing, 2013; pp 201–204. https://doi.org/10.1109/ISCAS.2013.6571817.
(29) Dong, J.; Jaramillo, R. Modeling Defect-Level Switching for Nonlinear and Hysteretic Electronic Devices. *Journal of Applied Physics* **2024**, *135* (22), 224501. https://doi.org/10.1063/5.0197121.

BRIEFS Observation of switching and neuromorphic behaviour in CdIn2S4-based devices controlled by native metastable defects.

SYNOPSIS

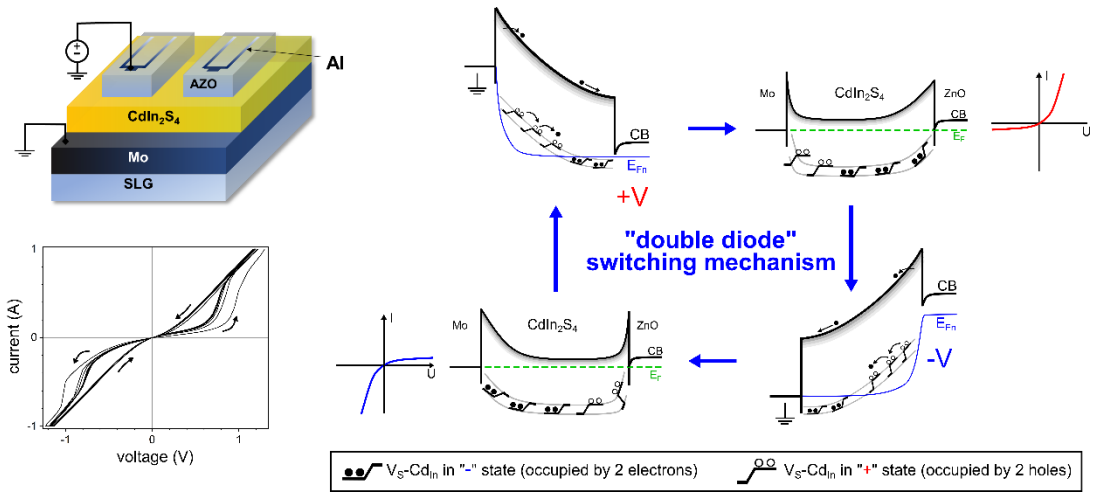

Figure: TOC